Science
AAAS

Supplementary Materials for

A long section of serpentinized depleted mantle peridotite

C. Johan Lissenberg *et al*.

Corresponding author: C. Johan Lissenberg, lissenbergcj@cardiff.ac.uk

Science **385**, 623 (2024)
DOI: 10.1126/science.adp1058

The PDF file includes:

Other Supplementary Material for this manuscript includes the following:

Materials and Methods

Materials and Methods

Rock description

Rock descriptions are based on combined core and thin section observations. Lithological units were designated on the basis of mineral proportions. For peridotite, we used the following subdivision based on orthopyroxene proportions: harzburgite (≥10% orthopyroxene); orthopyroxene-bearing dunite (1-10% orthopyroxene); dunite (<1% orthopyroxene).

Orthopyroxene proportions were estimated from macroscopic observations: because of their relatively large size and uneven distribution, macroscopic estimates were considered more reliable than thin section estimates. Clinopyroxene and Cr-spinel proportions were also estimated macroscopically, and olivine proportions were then calculated by subtraction. Due to low abundance, macroscopic estimates of clinopyroxene proportions are subject to uncertainty. To obtain a more robust estimate of clinopyroxene proportions, 'digital point counting' was performed on thirty thin sections. These thin sections were selected to be representative of the peridotites in Hole U1601C and were taken away from gabbroic intervals; they are closely associated with the samples selected for geochemical analyses (see below). Digital point counting comprised two steps: first, all clinopyroxene in thin sections was traced digitally on thin section scans. The resulting line drawings were then subject to image analysis to determine clinopyroxene proportions.

The extent of serpentinization is based on thin section observations of harzburgites, orthopyroxene-bearing dunites, and dunites. No thin sections were included that cross a contact with gabbros, magmatic veins or dikes. Modal abundances of each individual mineral and the extent of alteration for each mineral individually were estimated based on thin section observations. The total extent of serpentinization was then calculated using mass balance calculations using the estimated modal abundances of olivine, orthopyroxene and clinopyroxene and the extents of alteration of olivine, orthopyroxene and clinopyroxene.

The presence of carbonates in U1601C cores was determined in a collaborative fashion during shipboard description based on macroscopic observations. Systematic tests with hydrochloric acid (HCl) were performed throughout the borehole. With the exception of massive carbonate veins, carbonates were generally too small to be observed with a hand lens and are therefore inferred by reaction with acid. The carbonate mineralogy can only be confirmed in those locations where thin sections or X-ray diffraction analyses (XRD) are currently available. As Mg-carbonates (e.g., dolomite and magnesite) do not react to HCl, their presence or absence is not included in the carbonate distributions. As a consequence, the downhole carbonate estimation might be underestimated. Core observations were supplemented onshore by scanning electron microscope observations on selected samples, using a VEGA3 TESCAN Scanning Electron Microscope in backscatter electron imaging mode with an accelerating voltage of 20 kV and a working distance of 16.8 mm.

Whole-rock geochemistry

35 serpentinized peridotites were selected by the Expedition 399 Shipboard Scientific Party as representative of the rocks recovered at Site U1601 (6 at Hole U1601A and 29 at Hole U1601C) for shipboard bulk rock geochemical analyses. They comprised 31 harzburgites, two opx-bearing dunites and two dunites. A thin section or an XRD sample was located next to each geochemistry rock sample to determine its modal composition and degree of alteration.

The 35 serpentinized peridotite samples were prepared from 30 to 150 cm^3 of rock cut from cores and their outer surfaces cleaned to remove altered rinds resulting from drilling and cutting, then crushed according to the D/V JOIDES Resolution protocols (e.g., (*61*)). Crushed chips were ground to a fine powder using a SPEX 8515 Shatterbox powdering system with a tungsten carbide mill, except for five of the Hole U1601C samples that were powdered at Géosciences Montpellier using a Fritsch Pulverisette 2 with agate mortar and bowl. After powdering, each sample was ignited for 4 h at 1025°C to determine weight loss on ignition (LOI).

Bulk rock major and minor element analyses were conducted on splits of ignited powders using inductively coupled plasma optical emission spectroscopy (ICP-OES) on an Agilent 5110 spectrometer on-board D/V JOIDES Resolution for Hole U1601A samples and for 24 Hole U1601C samples, and on a Thermofisher iCAP Duo 7400 spectrometer at the AETE-ISO analytical facility (OSU OREME, University of Montpellier) for the five remaining Hole U1601C samples.

On board the D/V JOIDES Resolution, the digestion of rocks and subsequent ICP-OES analyses followed the protocol described in (*62*), summarized hereafter. 100.0 mg splits of whole-rock powders were mixed with $LiBO_2$ as a fluxer and LiBr as a non-wetting agent, then fused in Pt-Au crucibles in an internally rotating induction furnace (Bead Sampler NT-2100). The beads were dissolved in a 10% HNO_3 solution, then diluted to a dilution factor of ca. 5000. Be, In and Sb were used as an internal standard to correct for drift and matrix effects. Nine certified reference materials and one blank were prepared following the same protocol and used as calibration solutions.

At the AETE-ISO facility, 100 mg of rock powder was weighted and mixed with $LiBO_2$ and LiBr. Alkali fusion was conducted at 1000°C for 15 min using a Katanax X600 fluxer. After fluxing, the melt was mixed with 10% HNO_3 and diluted to a dilution factor of ca 2000. Sc was used as an internal standard. Six certified reference materials and one blank were prepared following the same protocol and used as calibration solutions.

Natural Gamma Radiation (NGR)

Gamma rays are emitted from rocks primarily as a result of the radioactive decay of ^{40}K and the decay of isotopes in the decay series of ^{238}U and ^{232}Th. The natural gamma radiation (NGR) of the in situ formation surrounding the borehole was determined by wireline logging. The Hostile Environment Natural Gamma Ray Sonde (HNGS; Schlumberger) measures natural radioactivity in the borehole wall using two bismuth germanate scintillation detectors. Concentrations of K, Th, and U, whose radioactive isotopes dominate the natural radiation spectrum, were computed by Schlumberger's proprietary spectroscopy method. The tool string was sent to the bottom of the hole while recording a partial set of data and was then pulled up at a constant speed (typically 250–500 m/h) to acquire the reported data.

The HNGS was deployed on four separate tool string deployments, yielding highly correlative profiles of computed K, Th, and U concentrations. In order to stabilize the drill string during wireline logging, the lowermost few tens of meters are stationary inside the borehole and the topmost 20-30 m of data logged through the pipe are invalid. The logging depth scale (WMSF = Wireline log matched depth below sea floor) is slightly different from the coring depth scale (typically up to a few dm discrepancy at any stratigraphic level) due to the different tools and methods used to measure and compute depth, respectively.

The HNGS Standard (total) Gamma Ray (HSGR) data is reported in standard gamma ray units of the American Petroleum Institute (gAPI). The HNGS Computed Gamma Ray (HCGR) data is the HSGR minus the uranium component.

Moisture and density (MAD)

Mass and volume measurements on discrete samples were made to determine bulk, dry, and grain density. The method is IODP standard for hard rocks and consists of a vacuum water saturator, a dual balance system, and a custom-built Helium hexapycnometer.
After saturating the cube samples with seawater, the wet mass was measured. The samples were subsequently dried in a 105°C oven for 24 h and then cooled to room temperature in a desiccator for 3 h, after which their dry mass was obtained for MAD measurements. The volume of the dry cube samples was then obtained using Helium pycnometry. Bulk density, dry density, and grain density were then calculated from wet mass, dry mass, and dry volume measurements using IODP Method C (*63*).

Dual balance system

A dual balance system was used to measure both wet and dry masses. Two analytical balances (Mettler-Toledo XS204) compensate for ship motion; one acts as a reference and the other measures the sample. The discrete samples were placed in aluminum trays, which were used to tare the reference and unknown balances. A standard mass of similar mass to that of the sample was placed on the reference balance to increase accuracy. Using a reference mass within ~10% of the sample mass, an accuracy of 0.005 g is readily attainable.

Hexapycnometer system

The hexapycnometer is an IODP custom-built system, using six Micromeritics cell units, custom electronics, and custom control programs. The system measures dry sample volume using pressurized Helium-filled chambers with a precision of 0.02 cm^3. For each measurement series, five cells contained unknowns and one cell contained two stainless steel calibration spheres (3 and 7 cm^3) with a total volume of ~10 cm^3. Calibration spheres were cycled through the cells to identify any systematic error and/or instrument drift. Spheres are assumed to be known to within 1% of their total volume. Three Helium purge cycles were carried out for each sample for increased accuracy.

Moisture and density calculations

For density calculations, both mass and volume are first corrected for the salt content of the pore fluid:

$$Ms = [S(Mw - Md)]/(1 - S) \quad (1)$$

where

- Ms = mass of salt,
- S = pore water salinity, (seawater with salinity 35 psu or 0.035 g/cm^3),
- Mw = wet mass of the sample, and
- Md = dry mass of the sample.

Grain density (ρg) is determined from the dry mass (Md) and dry volume (Vd) measurements:

$$\rho g = (Md - Ms)/[Vd - Ms/\rho s)] \quad (2)$$

where ρs is the density of salt (2.20 g/cm^3) (*63*).

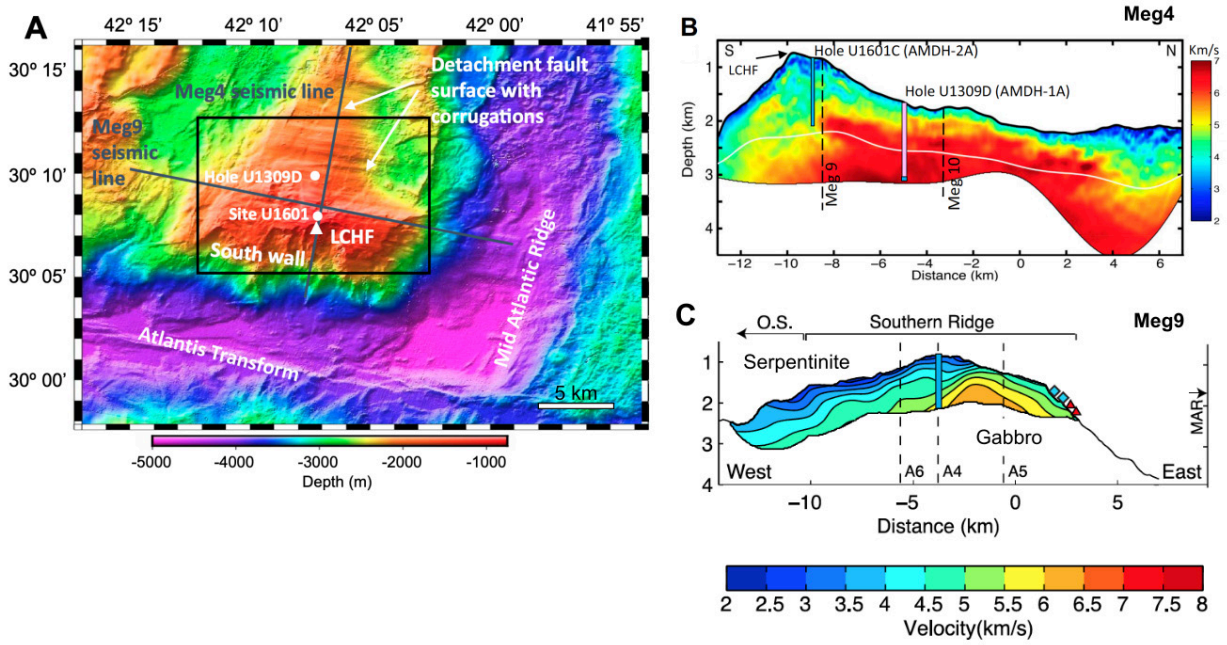

Fig. S1: The Atlantis Massif, seismic data, and IODP drilling. (**A**) Bathymetric map (*15*) showing the Atlantis Massif, seismic lines, the corrugated detachment fault surface, the Lost City hydrothermal field (LCHF) and IODP drilling locations. (**B**) Meg4 seismic line with full waveform inversion (FWI) processing, modified from (*64*). The solid white line marks the limit of the ray coverage for the tomographic inversion. Hole U1309D, drilled in IODP Expeditions 304/305 (*14*), was deepened by 80m during Expedition 399. Hole U1601C and a 55m pilot hole (U1601A) were drilled during Expedition 399. (**C**) Meg9 seismic line (*65*), with Hole 1601C shown. FWI has not been published for this line. In both this and Meg4, velocities >6km/s are assumed to be gabbro. Blue squares on the slope indicate dredge samples of gabbro exposed on the seafloor.

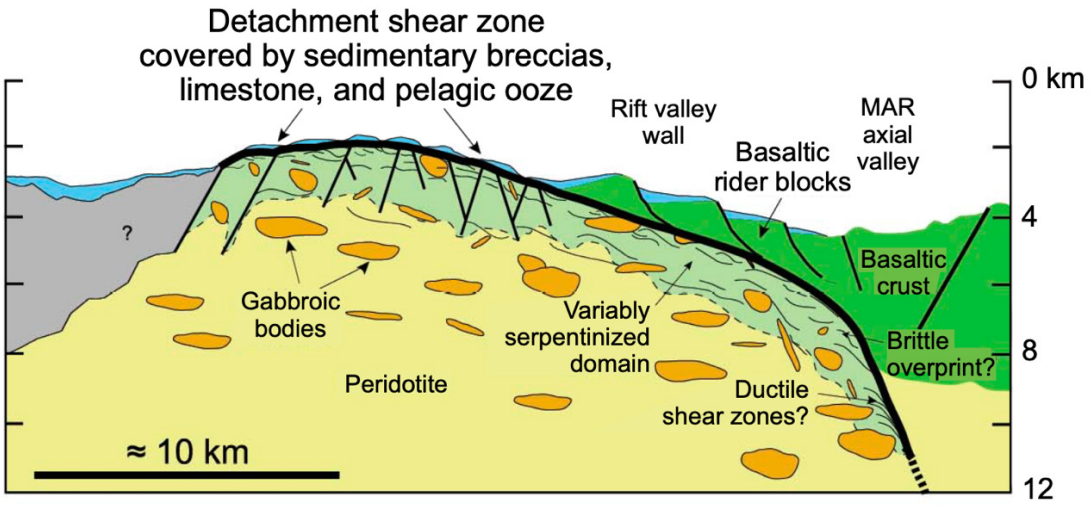

Fig. S2: Cross section of the South wall of Atlantis Massif. The South wall is dominated by variably altered peridotites with gabbroic lenses. Estimated 100 m thick detachment fault zone containing talc-tremolite-chlorite metasomatic schists is at the summit (*16*). In Expedition 399, the fault zone was found to be <30 m thick. MAR = Mid-Atlantic Ridge. Modified from (*66*).

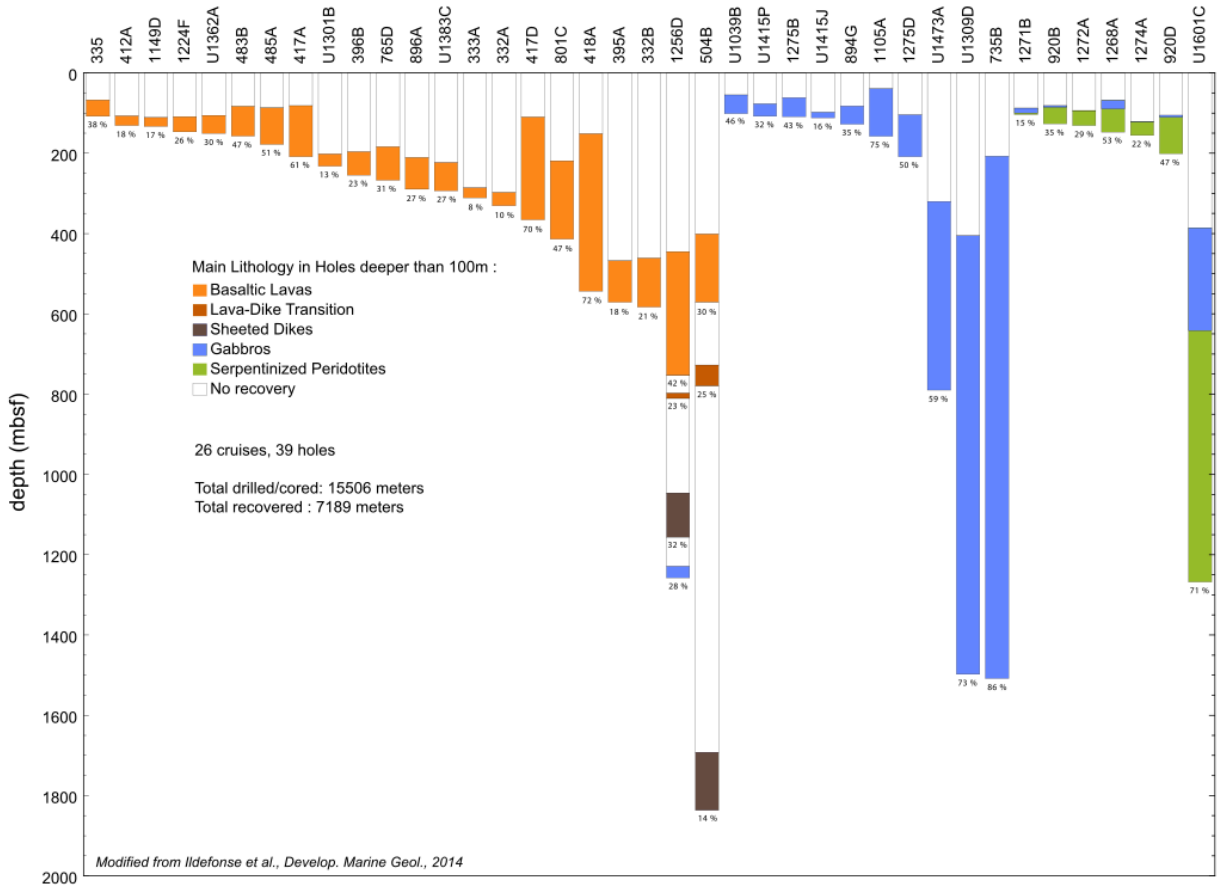

Fig. S3: Previous drilling of oceanic crust. Summary of all DSDP/ODP/IODP holes >100m in depth in igneous basement, modified from (*67*). Hole U1601C is more than six times as deep as the previous record in serpentinized peridotite.

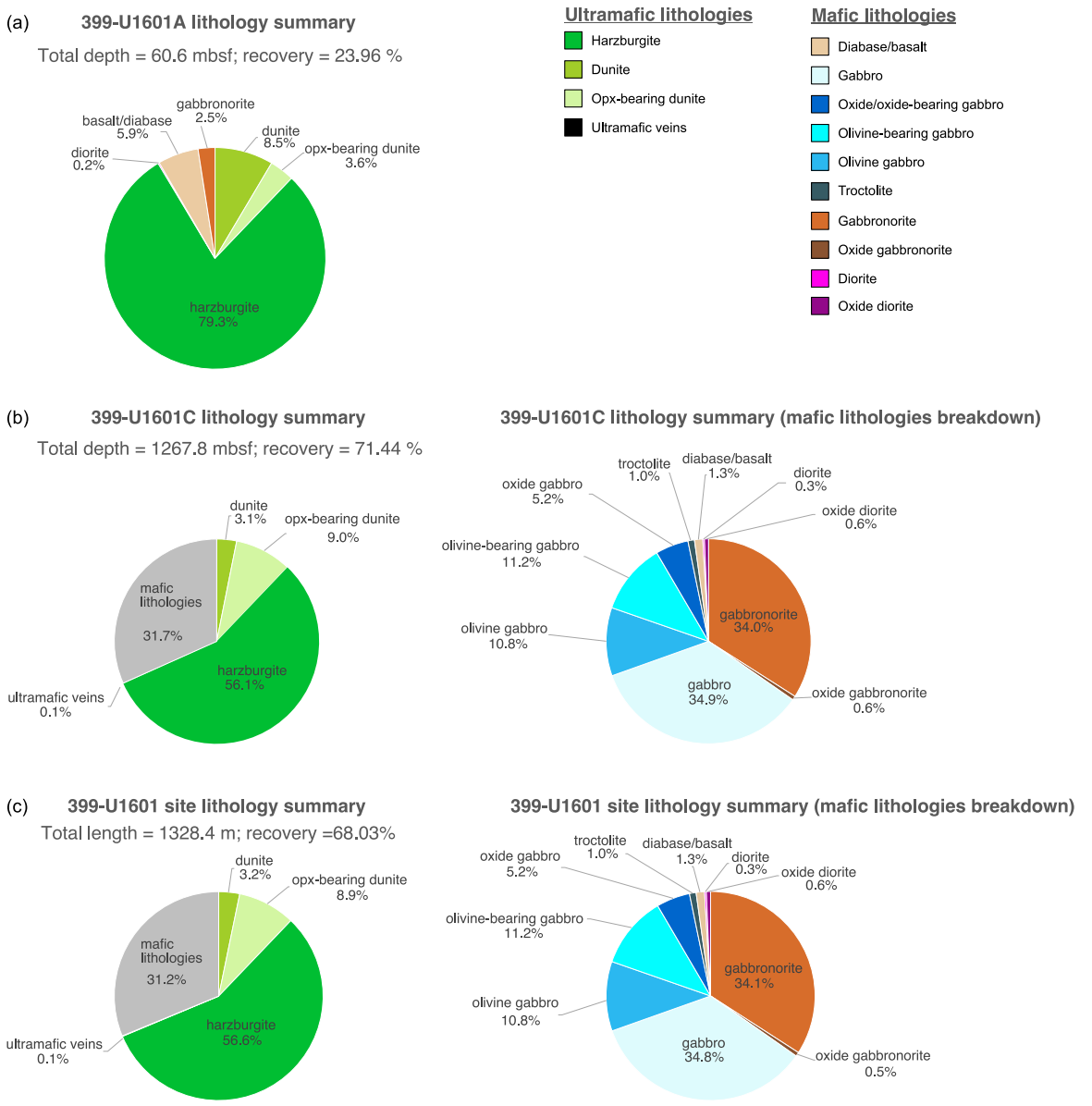

Fig. S4: lithological percentages of rocks recovered from Hole U1601A (A), Hole U1601C (B) and Site U1601 (C).

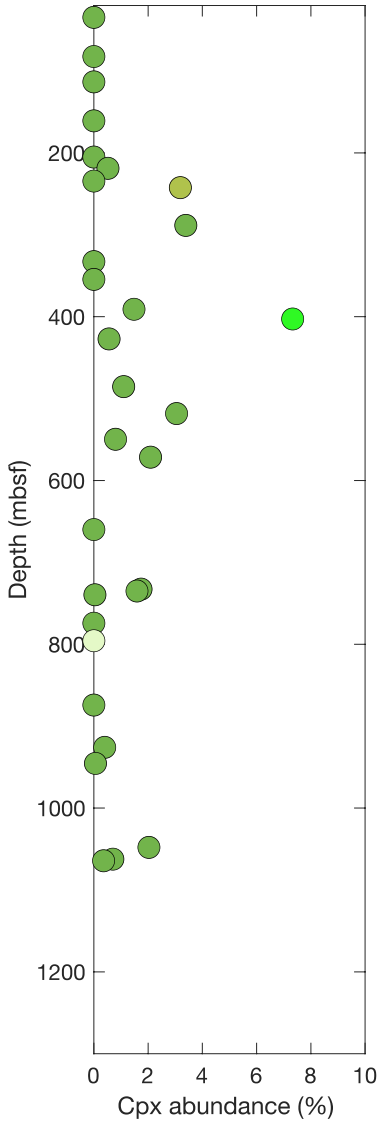

Fig. S5: Downhole model abundance (%) of clinopyroxene from digital point counting.

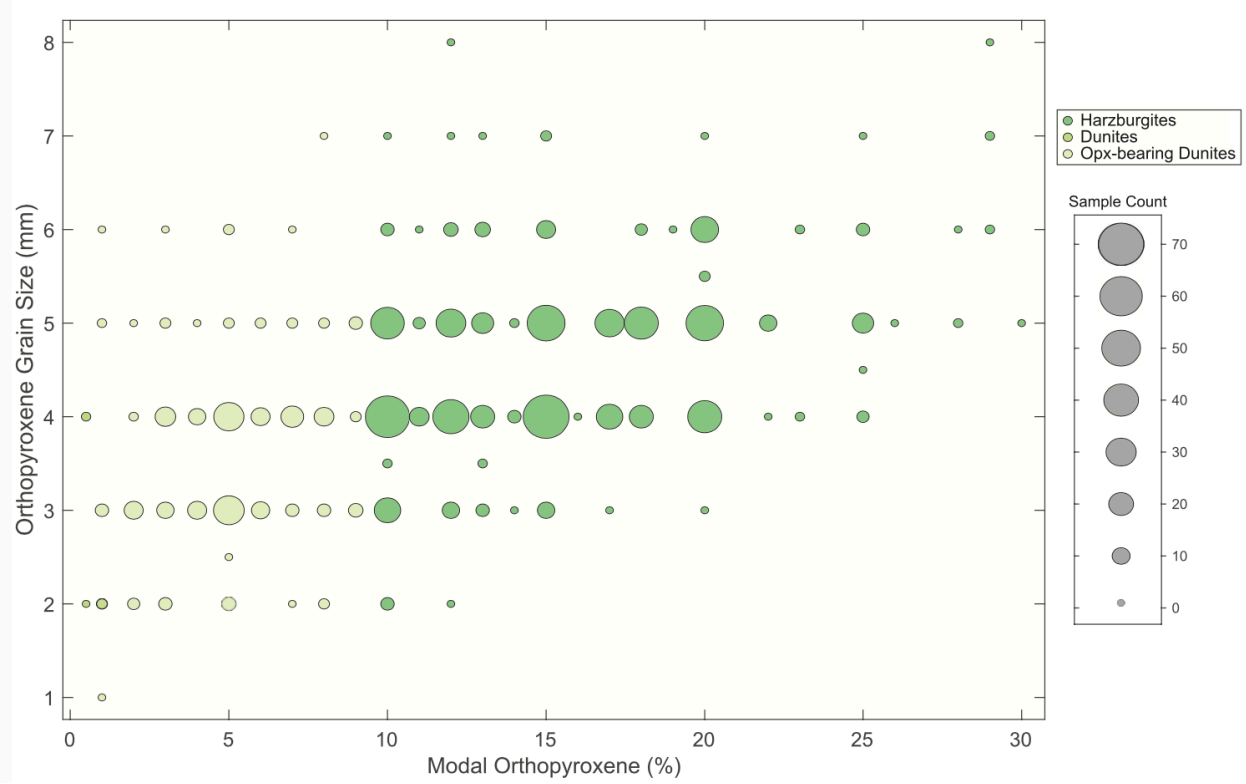

Fig. S6: Orthopyroxene size-abundance relationships. Data are for Hole U1601C harzburgite, opx-bearing dunite and dunite. Symbol size is proportional to number of datapoints.

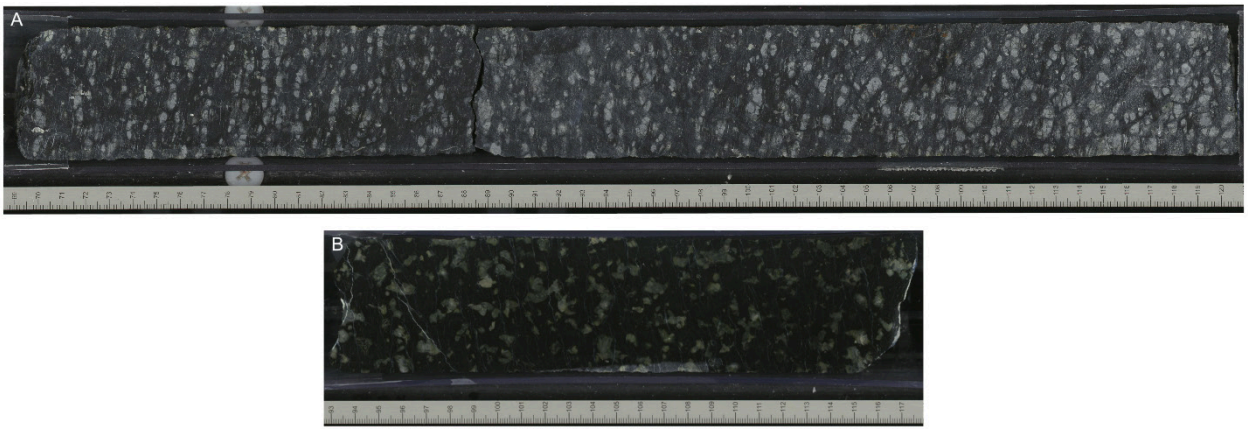

Fig. S7: Mantle fabrics. (A) Strongly foliated porphyroclastic harzburgite (Interval 399-U1601C-148R-3, 69 -121 cm). (**B)** Protogranular harzburgite (Interval 399-U1601C-113R-4, 93 -117 cm).

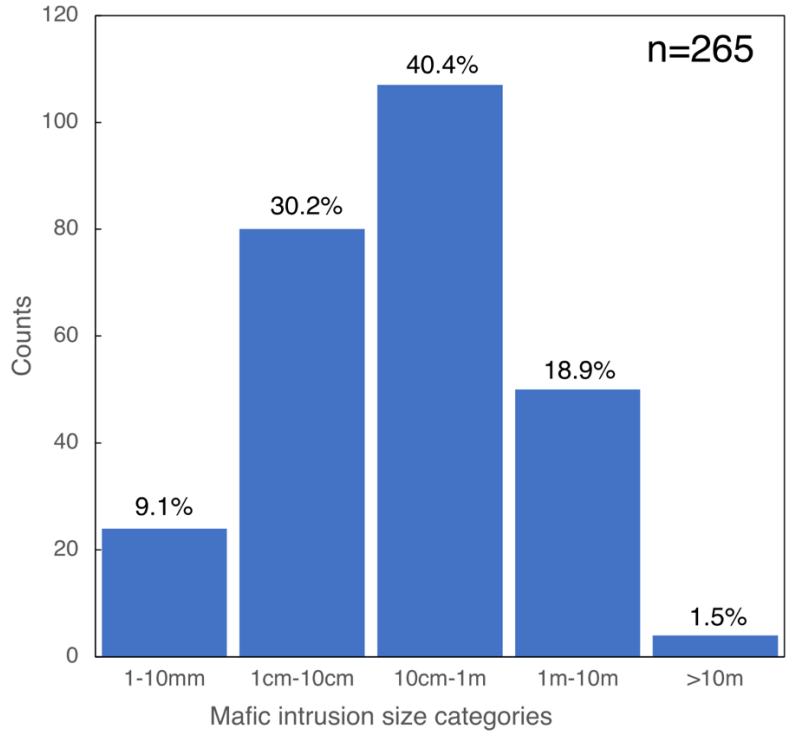

Fig. S8: Size distribution of gabbroic intrusions in Hole U1601C

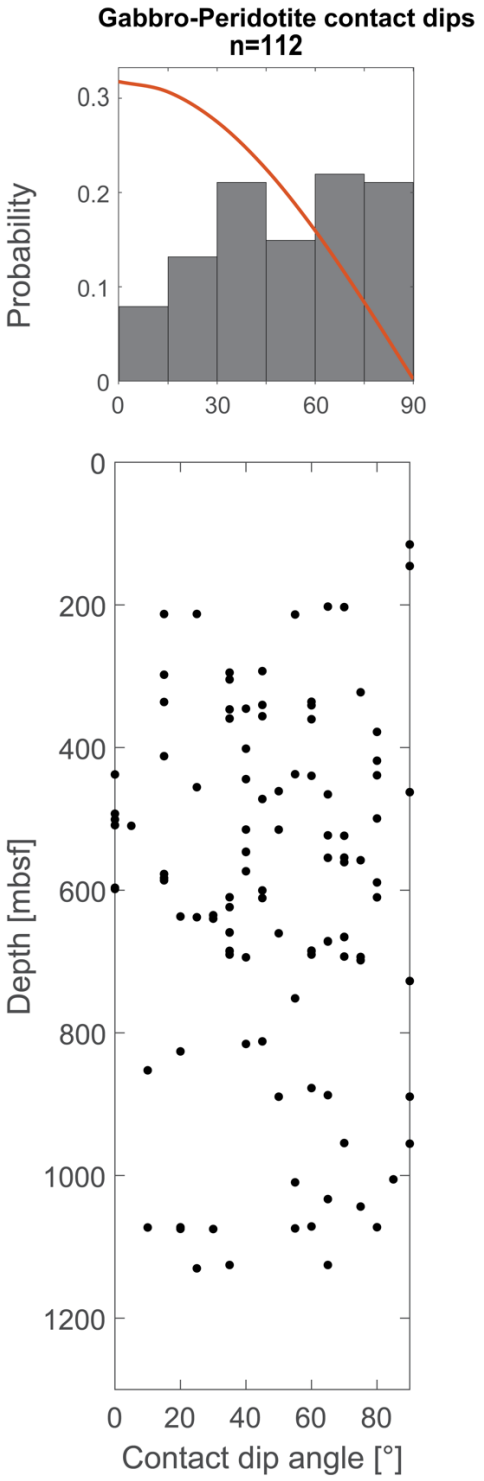

Fig. S9: Gabbro-peridotite dips. Histogram and downhole distribution of dip of gabbro-peridotite contacts in Hole U1601C. The distribution predicted for randomly orientated planes in drill core in red is superimposed on the histogram (*50*).

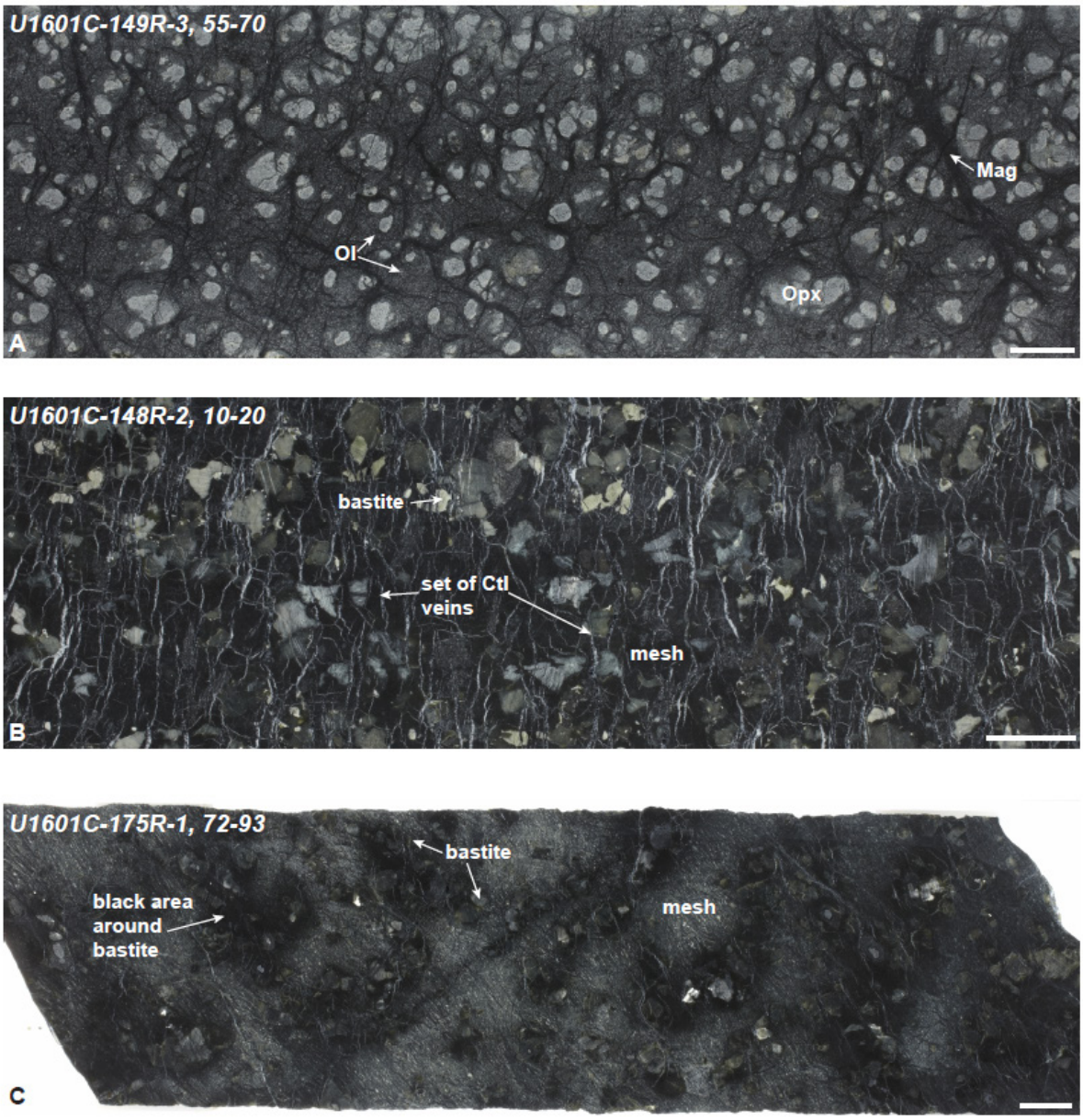

Fig. S10: Variably serpentinized peridotite in Hole U1601C. (**A)** Serpentinized harzburgite with common orthopyroxene and olivine relicts. Note that chrysotile veins are absent (Interval 399-U1601C-149R-3, 55-70 cm). (**B)** Highly serpentinized (~90%) harzburgite containing green and grey bastite after orthopyroxene. A set of white, fibrous to massive, subparallel horizontal ansgranular to locally paragranular chrysotile (Ctl) veins crosscuts the serpentinized harzburgite (Interval 399-U1601C-148R-2, 10-20 cm). (**C)** Highly serpentinized harzburgite (>90%) containing black and grey bastite after orthopyroxene. Black areas are commonly found around bastite. The serpentinite is cut by a few chrysotile veins (Interval 399-U1601C-175R-1, 72-93 cm). The white bar is 1 cm.

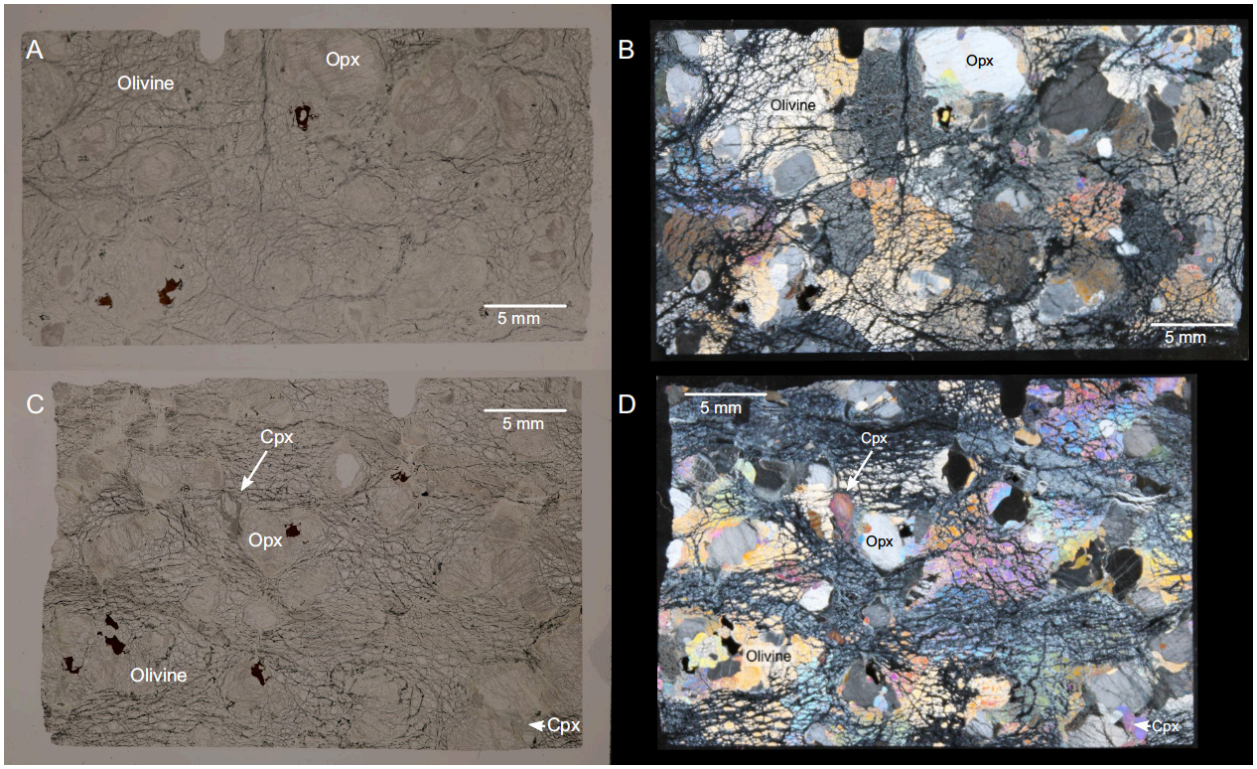

Fig. S11: Relatively fresh harzburgite. Whole thin section images (plane- and cross-polarized light) of Interval 399-U1601C-149R-3, 94-97 cm (**A, B)** and Interval 399-U1601C-148R-3, 118-121 cm (**C, D**) show abundant relict olivine and largely fresh orthopyroxene (opx) and sparse clinopyroxene (cpx) in harzburgite.

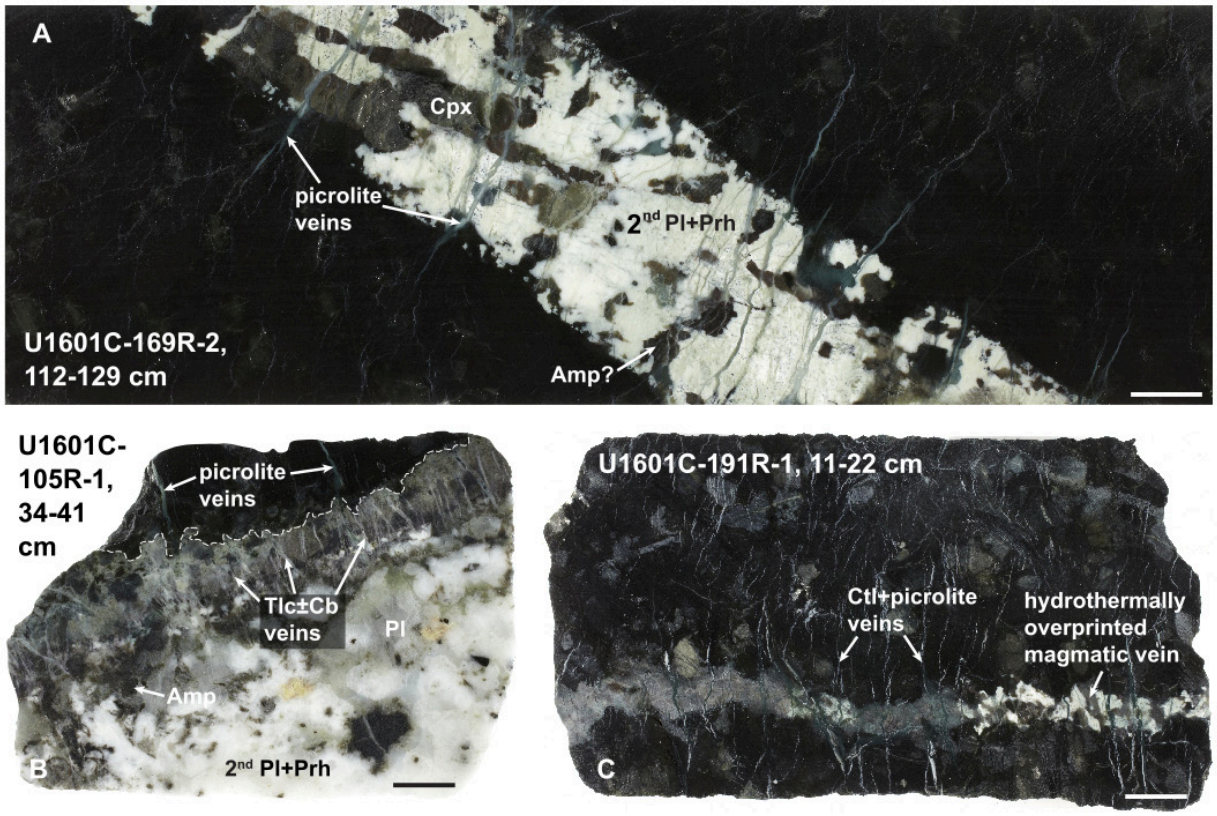

Fig. S12: Close-up images of the main vein type occurrences in serpentinized peridotites and at serpentinized peridotite-gabbroic rock contacts in Hole U1601C. (**A)** Hydrothermally overprinted magmatic vein composed of clinopyroxene (Cpx), amphibole (Amp?), prehnite (Prh), and secondary plagioclase (Pl) cut by a set of green massive picrolite veins (Interval 399-U1601C-169R-2, 112-129 cm). (**B)** Contact between serpentinized peridotite and altered gabbro (Interval 399-U1601C-105R-1, 34-41 cm). Set of talc (Tlc)-carbonate (Cb) veins branches at the contact and further continues in gabbro but not in serpentinite. A few picrolite veins cut through serpentinite and grade into prehnite veins when propagating in gabbro. (**C)** Hydrothermally overprinted magmatic vein cut by a set of composite chrysotile-picrolite veins (Interval 399-U1601C-191R-1, 11-22 cm). Picrolite vanishes away from magmatic vein.

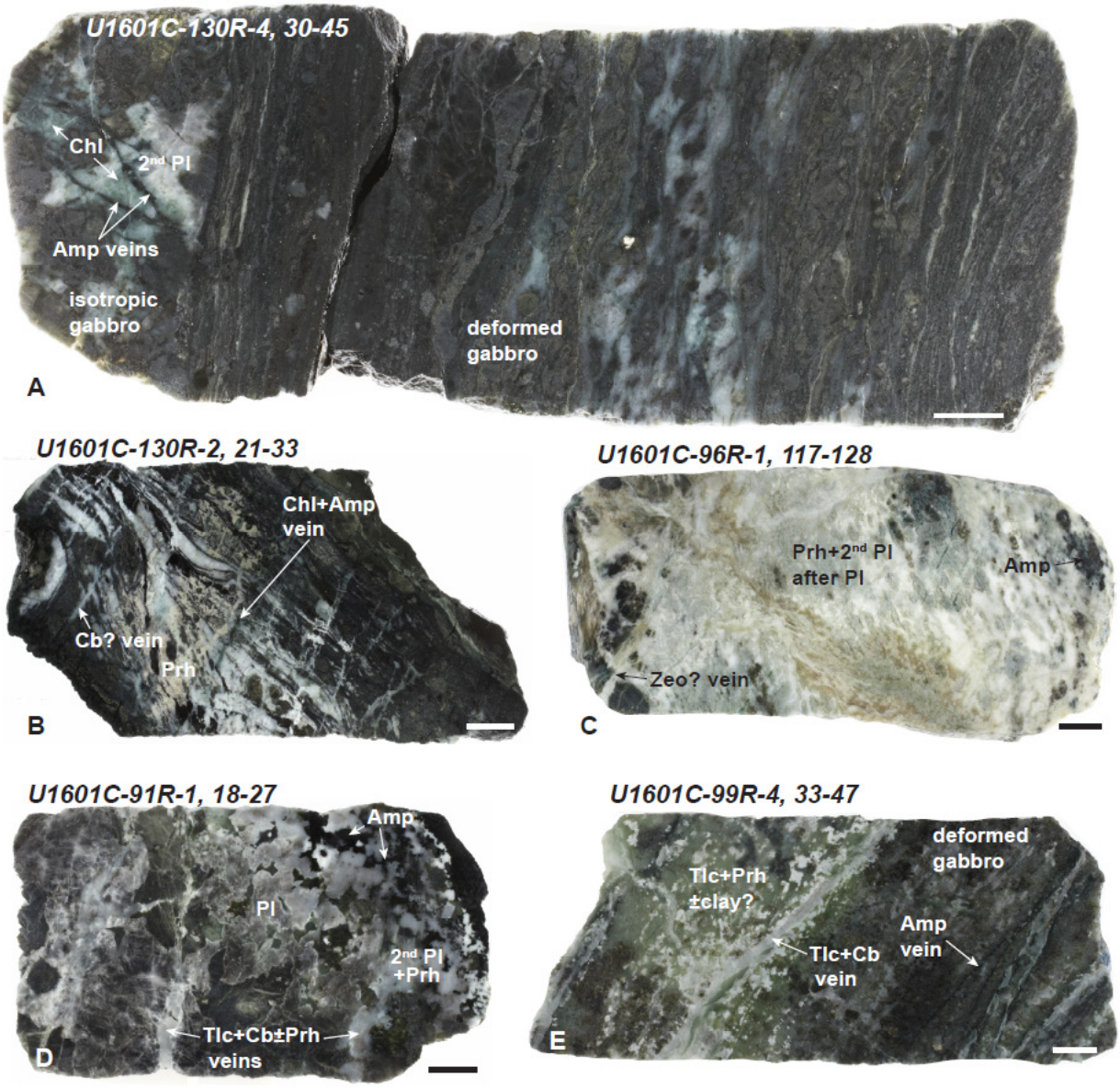

Fig S13. Close-up images of the main alteration features of gabbroic rocks in Hole U1601C. (**A)** Contact between a ductily-deformed and isotropic gabbro. Amphibole veins cut through the isotropic gabbro. Secondary plagioclase and chlorite form after plagioclase (Interval 399-U1601C-130R-4, 30-45 cm). (**B)** Highly deformed and altered (prehnite) gabbro cut by chlorite-amphibole veins overprinted by late carbonate(?) veins (Interval 399-U1601C-130R-2, 21-33 cm). (**C)** Highly altered and bleached gabbro composed of amphibole, secondary plagioclase, and prehnite and cut by late possible zeolite veins (Interval 399-U1601C-97R-1, 117-128 cm). (**D)** Contact between altered gabbro and serpentinized peridotite. Towards the contact, the degree of alteration in the gabbro increases and igneous minerals are completely replaced by amphibole, secondary plagioclase, and prehnite. It is cut by late talc-carbonate-prehnite veins (Interval 399-U1601C-91R-1, 18-27 cm). (**E)** Talc-carbonate veins cutting through a deformed gabbro. Talc, prehnite, and possibly clay minerals pervasively replace the gabbro at the vicinity of the veins (Interval 399-U1601C-99R-4, 33-47 cm). The scale bars are 1 cm.

Fig. S14: Highly weathered and serpentinized peridotite. Fe-(oxy)hydroxide veins locally reuse former serpentine veins and cut through the serpentine-magnetite veins (mesh network) and bastite suggesting weathering postdates serpentinization (Interval 399-U1601C-27R-1, 28-55 cm).

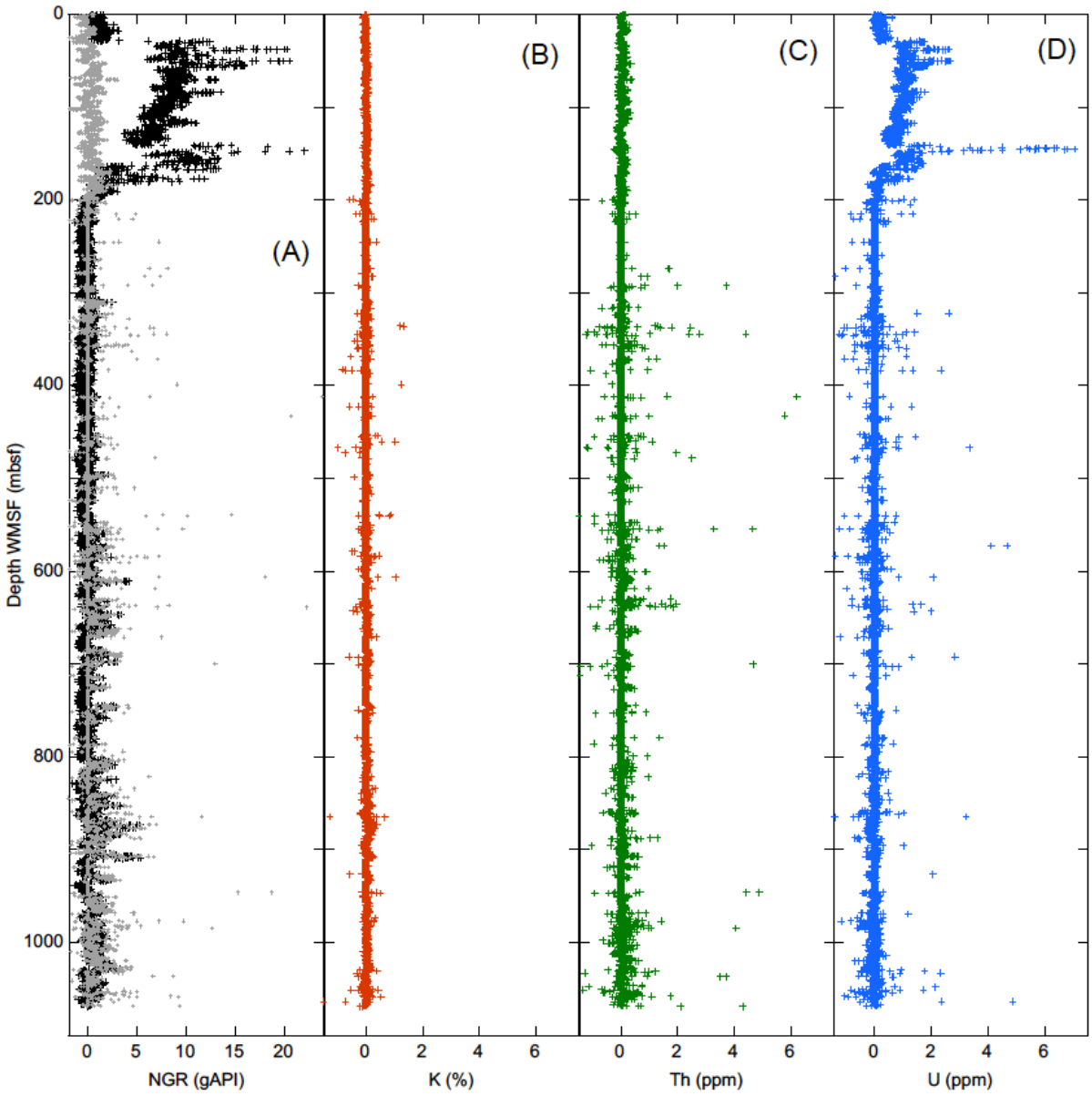

Figure S15. Wireline natural gamma ray (NGR) data. (A) Total signal (HSGR, black) and the computed signal without the uranium component (HCGR, gray). Concentrations of (B) potassium (C) thorium and (D) uranium computed by Schlumberger's proprietary spectroscopy method.

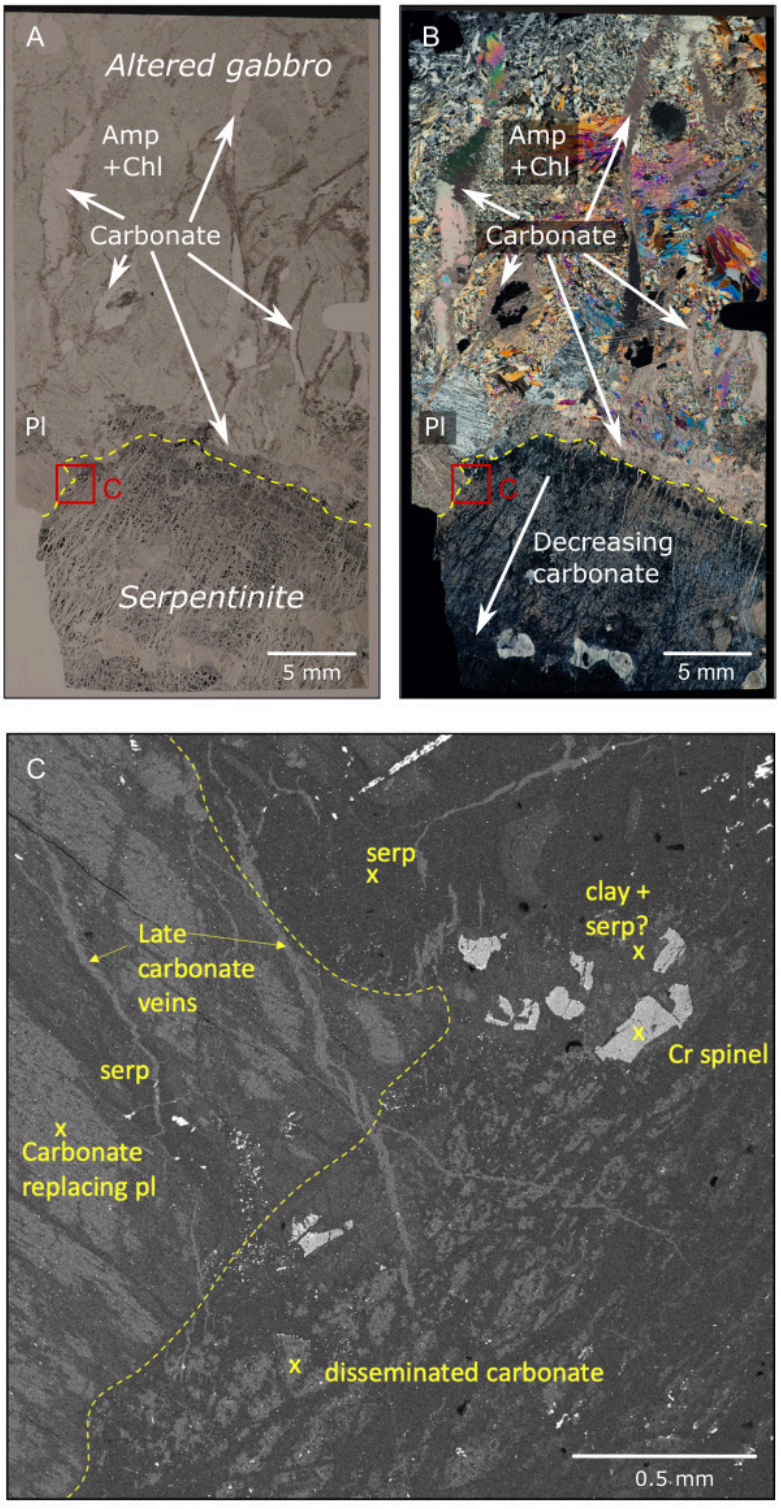

Fig. S16: Extensive carbonate veining and alteration in serpentinized peridotite and altered gabbro. Interval 399-U1601C-177R-1, 35-38 cm. (A)Whole thin section image (plane-polarized light) showing carbonate veins cutting gabbro completely altered to amphibole (Amp), chlorite (Chl), clay minerals, and locally secondary plagioclase, in contact with highly serpentinized peridotite. The contact is highlighted by the yellow dashed line. (B) Cross-polarized light image

showing coarse amphiboles and a relict plagioclase grain (Pl), altered to secondary plagioclase. Location of panel (C) is shown, and the decrease in disseminated and vein carbonate away from the contact can be seen by the reduction in birefringence. (C) Backscatter SEM image showing the boundary between gabbro and serpentinized peridotite. Disseminated calcium carbonate (EDS analysis shows no magnesite is present) is interpreted to overprint serpentine (serp) in the ultramafic layer. Cr-spinel is altered to serpentine and clay/chlorite. In the gabbro layer, a plagioclase grain (small relicts visible beyond the field of view) is almost completely altered to carbonate, serpentine, and probably chlorite. Thin carbonate veins cut the contact, indicating that they represent the latest event.

References and Notes

1. J. Korenaga, N. J. Planavsky, D. A. D. Evans, Global water cycle and the coevolution of the Earth's interior and surface environment. *Philos. Trans. A Math. Phys. Eng. Sci.* **375**, 20150393 (2017). doi:10.1098/rsta.2015.0393 Medline

2. R. Dasgupta, M. M. Hirschmann, The deep carbon cycle and melting in Earth's interior. *Earth Planet. Sci. Lett.* **298**, 1–13 (2010). doi:10.1016/j.epsl.2010.06.039

3. J. L. Charlou, J. P. Donval, C. Konn, H. Ondréas, Y. Fouquet, P. Jean-Baptiste, E. Fourré, "High production and fluxes of H_2 and CH_4 and evidence of abiotic hydrocarbon synthesis by serpentinization in ultramafic-hosted hydrothermal systems on the Mid-Atlantic Ridge" in *Diversity Of Hydrothermal Systems On Slow Spreading Ocean Ridges*, *Geophysical Monograph Series*, P. A. Rona, C. W. Devey, J. Dyment, B. J. Murton, Eds. (American Geophysical Union, 2010), vol. 188, pp. 265–296.

4. C. Neal, G. Stanger, Hydrogen generation from mantle source rocks in Oman. *Earth Planet. Sci. Lett.* **66**, 315–320 (1983). doi:10.1016/0012-821X(83)90144-9

5. T. M. McCollom, J. S. Seewald, Abiotic synthesis of organic compounds in deep-sea hydrothermal environments. *Chem. Rev.* **107**, 382–401 (2007). doi:10.1021/cr0503660 Medline

6. W. Martin, J. Baross, D. Kelley, M. J. Russell, Hydrothermal vents and the origin of life. *Nat. Rev. Microbiol.* **6**, 805–814 (2008). doi:10.1038/nrmicro1991 Medline

7. B.-X. Su, Q.-Q. Pan, Y. Xiao, J.-J. Jing, P. T. Robinson, I. Uysal, X. Liu, J.-G. Liu, Mantle peridotites of ophiolites rarely preserve reliable records of paleo-oceanic lithospheric mantle. *Earth Sci. Rev.* **244**, 104544 (2023). doi:10.1016/j.earscirev.2023.104544

8. E. S. Falk, P. B. Kelemen, Geochemistry and petrology of listvenite in the Samail ophiolite, Sultanate of Oman: Complete carbonation of peridotite during ophiolite emplacement. *Geochim. Cosmochim. Acta* **160**, 70–90 (2015). doi:10.1016/j.gca.2015.03.014

9. H. J. B. Dick, in *Magmatism in the Ocean Basins*, A. D. Saunders, M. J. Norry, Eds., Geological Society Special Publication (1989), vol. 42, pp. 71–105.

10. M. O. Schrenk, W. J. Brazelton, S. Q. Lang, Serpentinization, carbon, and deep life. *Rev. Mineral. Geochem.* **75**, 575–606 (2013). doi:10.2138/rmg.2013.75.18

11. J. M. Warren, Global variations in abyssal peridotite compositions. *Lithos* **248-251**, 193–219 (2016). doi:10.1016/j.lithos.2015.12.023

12. F. Klein, S. Humphris, W. Bach, Brucite formation and dissolution in oceanic serpentinite. *Geochem. Perspect. Lett.* **16**, 1–5 (2020). doi:10.7185/geochemlet.2035

13. M. Cannat *et al*., Eds., *Proc. ODP Init. Rep.* (Ocean Drilling Program, College Station, TX, 1995), vol. 153.

14. D. K. Blackman, B. Ildefonse, B. E. John, Y. Ohara, D. J. Miller, N. Abe, M. Abratis, E. S. Andal, M. Andreani, S. Awaji, J. S. Beard, D. Brunelli, A. B. Charney, D. M. Christie, J. Collins, A. G. Delacour, H. Delius, M. Drouin, F. Einaudi, J. Escartín, B. R. Frost, G. Früh-Green, P. B. Fryer, J. S. Gee, M. Godard, C. B. Grimes, A. Halfpenny, H.-E. Hansen, A. C. Harris, A. Tamura, N. W. Hayman, E. Hellebrand, T. Hirose, J. G. Hirth, S. Ishimaru, K. T. M. Johnson, G. D. Karner, M. Linek, C. J. MacLeod, J. Maeda, O. U.

Mason, A. M. McCaig, K. Michibayashi, A. Morris, T. Nakagawa, T. Nozaka, M. Rosner, R. C. Searle, G. Suhr, M. Tominaga, A. von der Handt, T. Yamasaki, X. Zhao, Drilling constraints on lithospheric accretion and evolution at Atlantis Massif, Mid-Atlantic Ridge 30°N. *J. Geophys. Res. Solid Earth* **116**, B07103 (2011). https://doi.org/10.1029/2010JB007931

15. J. Escartín, B. John, M. Cannat, J.-A. Olive, M. Cheadle, G. Früh-Green, C. Cotterill, Tectonic termination of oceanic detachment faults, with constraints on tectonic uplift and mass wasting related erosion rates. *Earth Planet. Sci. Lett.* **584**, 117449 (2022). doi:10.1016/j.epsl.2022.117449

16. J. Karson, G. L. Früh-Green, D. S. Kelley, E. A. Williams, D. R. Yoerger, M. Jakuba, Detachment shear zone of the Atlantis Massif core complex, Mid-Atlantic Ridge, 30°N. *Geochem. Geophys. Geosyst.* **7**, 2005GC001109 (2006). doi:10.1029/2005GC001109

17. D. S. Kelley, J. A. Karson, D. K. Blackman, G. L. Früh-Green, D. A. Butterfield, M. D. Lilley, E. J. Olson, M. O. Schrenk, K. K. Roe, G. T. Lebon, P. Rivizzigno; AT3-60 Shipboard Party, An off-axis hydrothermal vent field near the Mid-Atlantic Ridge at 30°N. *Nature* **412**, 145–149 (2001). doi:10.1038/35084000 Medline

18. W. J. Brazelton, M. O. Schrenk, D. S. Kelley, J. A. Baross, Methane- and sulfur-metabolizing microbial communities dominate the Lost City hydrothermal field ecosystem. *Appl. Environ. Microbiol.* **72**, 6257–6270 (2006). doi:10.1128/AEM.00574-06 Medline

19. D. S. Kelley, J. A. Karson, G. L. Früh-Green, D. R. Yoerger, T. M. Shank, D. A. Butterfield, J. M. Hayes, M. O. Schrenk, E. J. Olson, G. Proskurowski, M. Jakuba, A. Bradley, B. Larson, K. Ludwig, D. Glickson, K. Buckman, A. S. Bradley, W. J. Brazelton, K. Roe, M. J. Elend, A. Delacour, S. M. Bernasconi, M. D. Lilley, J. A. Baross, R. E. Summons, S. P. Sylva, A serpentinite-hosted ecosystem: The Lost City hydrothermal field. *Science* **307**, 1428–1434 (2005). doi:10.1126/science.1102556 Medline

20. S. Q. Lang, D. A. Butterfield, M. Schulte, D. S. Kelley, M. D. Lilley, Elevated concentrations of formate, acetate and dissolved organic carbon found at the Lost City hydrothermal field. *Geochim. Cosmochim. Acta* **74**, 941–952 (2010). doi:10.1016/j.gca.2009.10.045

21. G. Proskurowski, M. D. Lilley, D. S. Kelley, E. J. Olson, Low temperature volatile production at the Lost City Hydrothermal Field, evidence from a hydrogen stable isotope geothermometer. *Chem. Geol.* **229**, 331–343 (2006). doi:10.1016/j.chemgeo.2005.11.005

22. W. Seyfried Jr., N. J. Pester, B. M. Tutolo, K. Ding, The Lost City hydrothermal system: Constraints imposed by vent fluid chemistry and reaction path models on subseafloor heat and mass transfer processes. *Geochim. Cosmochim. Acta* **163**, 59–79 (2015). doi:10.1016/j.gca.2015.04.040

23. S. A. Whattam, G. L. Früh-Green, M. Cannat, J. C. M. De Hoog, E. M. Schwarzenbach, J. Escartin, B. E. John, M. I. Leybourne, M. J. Williams, S. Rouméjon, N. Akizawa, C. Boschi, M. Harris, K. Wenzel, A. McCaig, D. Weis, L. Bilenker, Geochemistry of serpentinized and multiphase altered Atlantis Massif peridotites (IODP Expedition 357): Petrogenesis and discrimination of melt-rock vs. fluid-rock processes. *Chem. Geol.* **594**, 120681 (2022). doi:10.1016/j.chemgeo.2021.120681

24. Y. Niu, Mantle Melting and Melt Extraction Processes beneath Ocean Ridges: Evidence from Abyssal Peridotites. *J. Petrol.* **38**, 1047–1074 (1997). doi:10.1093/petroj/38.8.1047

25. P. B. Kelemen, N. Shimizu, V. J. M. Salters, Extraction of mid-ocean-ridge basalt from the upwelling mantle by focused flow of melt in dunite channels. *Nature* **375**, 747–753 (1995). doi:10.1038/375747a0

26. Z. Morgan, Y. Liang, An experimental and numerical study of the kinetics of harzburgite reactive dissolution with applications to dunite dike formation. *Earth Planet. Sci. Lett.* **214**, 59–74 (2003). doi:10.1016/S0012-821X(03)00375-3

27. A. Morris, J. S. Gee, N. Pressling, B. E. John, C. J. MacLeod, C. B. Grimes, R. C. Searle, Footwall rotation in an oceanic core complex quantified using reoriented Integrated Ocean Drilling Program core samples. *Earth Planet. Sci. Lett.* **287**, 217–228 (2009). doi:10.1016/j.epsl.2009.08.007

28. B. J. deMartin, R. A. Sohn, J. Pablo Canales, S. E. Humphris, Kinematics and geometry of active detachment faulting beneath the Trans-Atlantic Geotraverse (TAG) hydrothermal field on the Mid-Atlantic Ridge. *Geology* **35**, 711–714 (2007). doi:10.1130/G23718A.1

29. C. J. MacLeod, R. C. Searle, B. J. Murton, J. F. Casey, C. Mallows, S. C. Unsworth, K. L. Achenbach, M. Harris, Life cycle of oceanic core complexes. *Earth Planet. Sci. Lett.* **287**, 333–344 (2009). doi:10.1016/j.epsl.2009.08.016

30. L. G. Montési, M. D. Behn, Mantle flow and melting underneath oblique and ultraslow mid-ocean ridges. *Geophys. Res. Lett.* **34**, 2007GL031067 (2007). doi:10.1029/2007GL031067

31. J.-A. Olive, *Dynamics of Plate Tectonics and Mantle Convection* (Elsevier, 2023), pp. 483–510.

32. D. W. Sparks, E. M. Parmentier, Melt extraction from the mantle beneath spreading centers. *Earth Planet. Sci. Lett.* **105**, 368–377 (1991). doi:10.1016/0012-821X(91)90178-K

33. R. F. Katz, S. M. Weatherley, Consequences of mantle heterogeneity for melt extraction at mid-ocean ridges. *Earth Planet. Sci. Lett.* **335–336**, 226–237 (2012). doi:10.1016/j.epsl.2012.04.042

34. P. B. Kelemen, M. Braun, G. Hirth, Spatial distribution of melt conduits in the mantle beneath oceanic spreading ridges: Observations from the Ingalls and Oman ophiolites. *Geochem. Geophys. Geosyst.* **1**, 1999GC000012 (2000). doi:10.1029/1999GC000012

35. D. E. Allen, W. Seyfried Jr., Compositional controls on vent fluids from ultramafic-hosted hydrothermal systems at mid-ocean ridges: An experimental study at 400 C, 500 bars. *Geochim. Cosmochim. Acta* **67**, 1531–1542 (2003). doi:10.1016/S0016-7037(02)01173-0

36. F. Klein, W. Bach, S. E. Humphris, W.-A. Kahl, N. Jons, B. Moskowitz, T. S. Berquo, Magnetite in seafloor serpentinite—Some like it hot. *Geology* **42**, 135–138 (2014). doi:10.1130/G35068.1

37. C. Boschi, A. Dini, G. L. Früh-Green, D. S. Kelley, Isotopic and element exchange during serpentinization and metasomatism at the Atlantis Massif (MAR 30 N): Insights from B and Sr isotope data. *Geochim. Cosmochim. Acta* **72**, 1801–1823 (2008). doi:10.1016/j.gca.2008.01.013

38. S. Rouméjon, G. L. Früh-Green, B. N. Orcutt; the IODP Expedition Party, Alteration heterogeneities in peridotites exhumed on the southern wall of the Atlantis Massif (IODP Expedition 357). *J. Petrol.* **59**, 1329–1358 (2018). doi:10.1093/petrology/egy065

39. J. Kodolányi, T. Pettke, C. Spandler, B. S. Kamber, K. Gméling, Geochemistry of ocean floor and fore-arc serpentinites: Constraints on the ultramafic input to subduction zones. *J. Petrol.* **53**, 235–270 (2012). doi:10.1093/petrology/egr058

40. M. Seitz, S. Hart, Uranium and boron distributions in some oceanic ultramafic rocks. *Earth Planet. Sci. Lett.* **21**, 97–107 (1973). doi:10.1016/0012-821X(73)90230-6

41. J. C. Alt, E. M. Schwarzenbach, G. L. Früh-Green, W. C. Shanks III, S. M. Bernasconi, C. J. Garrido, L. Crispini, L. Gaggero, J. A. Padrón-Navarta, C. Marchesi, The role of serpentinites in cycling of carbon and sulfur: Seafloor serpentinization and subduction metamorphism. *Lithos* **178**, 40–54 (2013). doi:10.1016/j.lithos.2012.12.006

42. S. Pujatti, O. Plümper, B. M. Tutolo, Weathering-driven porosity generation in altered oceanic peridotites. *Earth Planet. Sci. Lett.* **604**, 118006 (2023). doi:10.1016/j.epsl.2023.118006

43. E. M. Schwarzenbach, G. L. Früh-Green, S. M. Bernasconi, J. C. Alt, A. Plas, Serpentinization and carbon sequestration: A study of two ancient peridotite-hosted hydrothermal systems. *Chem. Geol.* **351**, 115–133 (2013). doi:10.1016/j.chemgeo.2013.05.016

44. J. E. Snow, H. J. B. Dick, Pervasive magnesium loss by marine weathering of peridotite. *Geochim. Cosmochim. Acta* **59**, 4219–4235 (1995). doi:10.1016/0016-7037(95)00239-V

45. L. Ternieten, G. L. Früh-Green, S. M. Bernasconi, Distribution and sources of carbon in serpentinized mantle peridotites at the Atlantis Massif (IODP Expedition 357). *J. Geophys. Res. Solid Earth* **126**, e2021JB021973 (2021). doi:10.1029/2021JB021973

46. K. A. Ludwig, D. S. Kelley, D. A. Butterfield, B. K. Nelson, G. Früh-Green, Formation and evolution of carbonate chimneys at the Lost City Hydrothermal Field. *Geochim. Cosmochim. Acta* **70**, 3625–3645 (2006). doi:10.1016/j.gca.2006.04.016

47. D. E. Allen, W. Seyfried Jr., Serpentinization and heat generation: Constraints from Lost City and Rainbow hydrothermal systems. *Geochim. Cosmochim. Acta* **68**, 1347–1354 (2004). doi:10.1016/j.gca.2003.09.003

48. S. Q. Lang, G. L. Früh-Green, S. M. Bernasconi, M. D. Lilley, G. Proskurowski, S. Méhay, D. A. Butterfield, Microbial utilization of abiogenic carbon and hydrogen in a serpentinite-hosted system. *Geochim. Cosmochim. Acta* **92**, 82–99 (2012). doi:10.1016/j.gca.2012.06.006

49. J. L. Palandri, M. H. Reed, Geochemical models of metasomatism in ultramafic systems: Serpentinization, rodingitization, and sea floor carbonate chimney precipitation. *Geochim. Cosmochim. Acta* **68**, 1115–1133 (2004). doi:10.1016/j.gca.2003.08.006

50. S. J. Martel, Analysis of fracture orientation data from boreholes. *Environ. Eng. Geosci.* **V**, 213–233 (1999). doi:10.2113/gseegeosci.V.2.213

51. M. Godard, S. Awaji, H. Hansen, E. Hellebrand, D. Brunelli, K. Johnson, T. Yamasaki, J. Maeda, M. Abratis, D. Christie, Y. Kato, C. Mariet, M. Rosner, Geochemistry of a long in-situ section of intrusive slow-spread oceanic lithosphere: Results from IODP Site

U1309 (Atlantis Massif, 30∞N Mid-Atlantic-Ridge). *Earth Planet. Sci. Lett.* **279**, 110–122 (2009). doi:10.1016/j.epsl.2008.12.034

52. R. K. Workman, S. R. Hart, Major and trace element composition of the depleted MORB mantle (DMM). *Earth Planet. Sci. Lett.* **231**, 53–72 (2005). doi:10.1016/j.epsl.2004.12.005

53. E. Jagoutz, H. Palme, H. Baddenhausen, K. Blum, M. Cendales, G. Dreibus, B. Spettel, V. Lorenz, H. Wänke, in *Proceedings of the 10th Lunar and Planetary Science Conference*, Houston, TX, 19 to 23 March 1979 (Pergamon, 1979), vol. 2, pp. 2031–2050.

54. S. R. Hart, A. Zindler, In search of a bulk-earth composition. *Chem. Geol.* **57**, 247–267 (1986). doi:10.1016/0009-2541(86)90053-7

55. W. F. McDonough, S. Sun, The composition of the Earth. *Chem. Geol.* **120**, 223–253 (1995). doi:10.1016/0009-2541(94)00140-4

56. J. F. Casey, in *Proc. ODP, Sci. Res.*, J. A. Karson, M. Cannat, D. J. Miller, D. Elthon, Eds. (Ocean Drilling Program, College Station, TX, 1997), vol. 153, pp. 181–241.

57. M. Godard, Y. Lagabrielle, O. Alard, J. Harvey, Geochemistry of the highly depleted peridotites drilled at ODP Sites 1272 and 1274 (Fifteen-Twenty Fracture Zone, Mid-Atlantic Ridge): Implications for mantle dynamics beneath a slow spreading ridge. *Earth Planet. Sci. Lett.* **267**, 410–425 (2008). doi:10.1016/j.epsl.2007.11.058

58. H. Paulick, W. Bach, M. Godard, J. C. M. De Hoog, G. Suhr, J. Harvey, Geochemistry of abyssal peridotites (Mid-Atlantic Ridge, 15 20′ N, ODP Leg 209): Implications for fluid/rock interaction in slow spreading environments. *Chem. Geol.* **234**, 179–210 (2006). doi:10.1016/j.chemgeo.2006.04.011

59. J.-L. Bodinier, M. Godard, Orogenic, ophiolitic, and abyssal peridotites. *Treatise Geochem.* **2**, 103–170 (2003).

60. C. B. Grimes, B. E. John, M. Cheadle, J. L. Wooden, Protracted construction of gabbroic crust at a slow-spreading ridge: Constraints from 206Pb/238U zircon ages from Atlantis Massif and IODP Hole U1309D (30°N, MAR). *Geochem. Geophys. Geosyst.* **9**, 2008GC002063 (2008). doi:10.1029/2008GC002063

61. R. M. Coggon, D. A. H. Teagle, J. B. Sylvan, J. Reece, E. R. Estes, T. J. Williams, G. L. Christeson, M. Aizawa, E. Albers, C. Amadori, T. M. Belgrano, C. Borrelli, J. D. Bridges, E. J. Carter, T. D'Angelo, J. Dinarès-Turell, N. Doi, J. D. Estep, A. Evans, W. P. Gilhooly III, L. J. C. Grant, G. M. Guérin, M. Harris, V. M. Hojnacki, G. Hong, X. Jin, M. Jonnalagadda, M. R. Kaplan, P. D. Kempton, D. Kuwano, J. M. Labonte, A. R. Lam, M. Latas, C. M. Lowery, W. Lu, A. McIntyre, P. Moal-Darrigade, S. F. Pekar, C. Robustelli Test, C. M. Routledge, J. G. Ryan, D. Santiago Ramos, A. Shchepetkina, A. L. Slagle, M. Takada, L. Tamborrino, A. Villa, Y. Wang, S. Y. Wee, S. J. Widlansky, K. Yang, W. Kurz, M. Prakasam, L. Tian, T. Yu, G. Zhang, "Expedition 390/393 methods" in *Proceedings of the International Ocean Discovery Program*, 390/393, College Station, TX (International Ocean Discovery Program, 2024), R. M. Coggon, D. A. H. Teagle, J. B. Sylvan, J. Reece, E. R. Estes, T. J. Williams, G. L. Christeson, and the Expedition 390/393 Scientists, South Atlantic Transect; https://doi.org/10.14379/iodp.proc.390393.102.2024.

62. R. Murray, D. J. Miller, K. Kryc, Analysis of major and trace elements in rocks, sediments, and interstitial waters by inductively coupled plasma–atomic emission spectrometry (ICP-AES). *ODP Technical Note* **29** (2000). doi:10.2973/odp.tn.29.2000

63. P. Blum, Physical properties handbook—A guide to the shipboard measurement of physical properties of deep-sea cores. *ODP Tech. Note* **26** (1997). doi:10.2973/odp.tn.26.1997

64. A. J. Harding, A. F. Arnulf, D. K. Blackman, Velocity structure near IODP Hole U1309D, Atlantis Massif, from waveform inversion of streamer data and borehole measurements. *Geochem. Geophys. Geosyst.* **17**, 1990–2014 (2016). doi:10.1002/2016GC006312

65. A. Henig, D. K. Blackman, A. J. Harding, J. P. Canales, G. M. Kent, Downward continued multichannel seismic refraction analysis of Atlantis Massif oceanic core complex, 30° N, Mid-Atlantic Ridge. *Geochem. Geophys. Geosyst.* **13**, 2012GC004059 (2012). doi:10.1029/2012GC004059

66. C. Boschi, G. L. Früh-Green, A. Delacour, J. A. Karson, D. S. Kelley, Mass transfer and fluid flow during detachment faulting and development of an oceanic core complex, Atlantis Massif (MAR 30 N). *Geochem. Geophys. Geosyst.* **7**, 2005GC001074 (2006). doi:10.1029/2005GC001074

67. B. Ildefonse, N. Abe, M. Godard, A. Morris, D. A. H. Teagle, S. Umino, "Formation and evolution of oceanic lithosphere: new insights on crustal structure and igneous geochemistry from ODP/IODP sites 1256, U1309, and U1415" in *Earth and Life Processes Discovered from Subseafloor Environments*, vol. 7 of *Developments in Marine Geology*, R. Stein, D. K. Blackman, F. Inagaki, H.-C. Larsen, Eds. (Elsevier, 2014), pp. 449–505.